



Article

# The Stabilizing of 1T-MoS<sub>2</sub> for All-Solid-State Lithium-Ion Batteries

Peidian Chong<sup>1</sup> , Ziwang Zhou<sup>1</sup>, Kaihong Wang<sup>1</sup>, Wenhao Zhai<sup>2</sup>, Yafeng Li<sup>1,\*</sup>, Jianbiao Wang<sup>2,\*</sup> , and Mingdeng Wei<sup>1,\*</sup>

<sup>1</sup> Fujian Key Laboratory of Electrochemical Energy Storage Materials, Fuzhou University, Fuzhou 350116, China

<sup>2</sup> Agency for Science, Technology and Research (A\*STAR), Innovis, Institute of Materials Research and Engineering, Singapore 138634, Singapore

\* Correspondence: liyf@fzu.edu.cn (Y.L.); jianbiao\_wang@imre.a-star.edu.sg (J.W.); wei-mingdeng@fzu.edu.cn (M.W.)

**Abstract:** All-solid-state batteries (SSBs) are prospective candidates for a range of energy accumulation systems, delivering higher energy densities compared to batteries which use liquid electrolytes. Amongst the numerous solid-state electrolytes (SEs), sulfide-based electrolytes in particular have received more attention given that they have a high ionic conductivity. However, the incompatibility between the electrode and SEs is still an ongoing challenge that leads to poor electrochemical performance. In this work, we focus on 1T-MoS<sub>2</sub>. It is well known that 1T metallic MoS<sub>2</sub> is unstable even at room temperature. However, we showed that 1T-MoS<sub>2</sub> can be stabilized at 600 °C for at least 2 h, and the 1T-MoS<sub>2</sub>-600 interlayer spacing expanded to 0.95 nm. The high crystallinity of the 1T phase is highly compatible with solid electrolytes and coupled with the increased interlayer spacing, so in the all-solid-state lithium-ion battery (ALLLIB), we achieved outstanding cycling performance. At the current density of 0.2 C (1 C = 670 mA g<sup>-1</sup>), this material delivered a capacity of 406 mA h g<sup>-1</sup> after 50 cycles.

**Keywords:** 1T metallic; MoS<sub>2</sub>; high crystalline; lithium-ion battery; all-solid-state



**Citation:** Chong, P.; Zhou, Z.; Wang, K.; Zhai, W.; Li, Y.; Wang, J.; Wei, M. The Stabilizing of 1T-MoS<sub>2</sub> for All-Solid-State Lithium-Ion Batteries. *Batteries* **2023**, *9*, 26. <https://doi.org/10.3390/batteries9010026>

Academic Editor: Hirotooshi Yamada

Received: 21 November 2022

Revised: 22 December 2022

Accepted: 28 December 2022

Published: 29 December 2022



**Copyright:** © 2022 by the authors. Licensee MDPI, Basel, Switzerland. This article is an open access article distributed under the terms and conditions of the Creative Commons Attribution (CC BY) license (<https://creativecommons.org/licenses/by/4.0/>).

## 1. Introduction

As renewable source of energy devices, lithium-ion batteries have been widely applied to replace traditional fossil resources [1–7]. Unfortunately, the combustibility of organic liquid electrolytes is a serious fire hazard which raises safety concerns [8–13]. To this end, solid electrolytes (SEs) were proposed as a solution due to their nonflammable characteristics and comparable ionic conductivity, especially in sulfide-based electrolytes, because they have a high ionic conductivity [14–19]. However, the compatibility between the electrode and SEs is still an ongoing challenge and impedes the progression of ASSLIB [20–26]. Selecting a suitable electrode material that is compatible with SEs has become essential and urgent for enhancing the electrochemical performance of ASSLIBs. Two-dimensional transition metal dichalcogenides (2D TMDs) such as 2D Molybdenum disulfide (MoS<sub>2</sub>) are regarded as promising candidates for ASSLIBs among the various electrode materials, owing to their intrinsically higher ionic conductivity, large layer spacing and compatibility with sulfide-based SEs [27–29]. The application of these materials in energy storage has been intensively researched such as sodium-ion batteries, ALLLIBs, zinc-ion batteries etc. [30–33]. However, their noticeable volume variation and the poor conductivity of electricity in charge/discharge process impedes further application of MoS<sub>2</sub>. Due to these constraints, nanostructural 1T-MoS<sub>2</sub> which has a more stable electrochemical performance has been suggested as the solution. MoS<sub>2</sub> has three different phases including 1T, 2H, and 3R. Many reports have researched 2H and 3R phases of MoS<sub>2</sub>. Additionally, a new problem arises, because it is well known that metastable phase 1T-MoS<sub>2</sub> is unstable and degrades into its 2H even at room temperature. In previous works, Santhosha et al. [34]

investigated exfoliated MoS<sub>2</sub> as the electrode of ASSLIBs, the nanosized electrode materials could reduce the volume expansion and enhance the compatibility with SEs, so the capacity of 312 mA h g<sup>-1</sup> at a current density of 0.1 C was maintained after 500 cycles. Li et al. [35] adopted O-doping and structure defects manufacturing to produce abundant 1T-MoS<sub>2</sub>(D-MoS<sub>2</sub>-O), metallic 1T-MoS<sub>2</sub> can improve the conductivity and the expanded planes availed the diffusion of Zn<sup>2+</sup>, so they had tailored this material with long cycling durability and high-rate capability. Mirabal et al. [36] used a simple procedure to create PEO intercalation MoS<sub>2</sub> composites, additionally, the increase electrochemical performance proved that interlayer expansion is a successful method for creating high-performance anode materials for ion store battery technologies.

In this work, we overcome the bottleneck of 1T-MoS<sub>2</sub> degrading into its 2H phase even at high temperatures by using facile solvothermal synthesis method. By doing so, 1T-MoS<sub>2</sub> with a stable phase can be obtained and the resulting compound remains phase-stable even at temperatures as high as 600 °C. Furthermore, the interlayer spacing of 1T-MoS<sub>2</sub> expands to 0.95 nm, contrary to 1T-MoS<sub>2</sub>-200 is 0.62 nm. These expanded planes availed the diffusion of Li<sup>+</sup> [37]. Furthermore, owing to that the higher crystallinity was favored for the compatibility between the electrode and SEs, our facile solvothermal synthesized 1T-MoS<sub>2</sub> also exhibited a superior electrochemical performance. A capacity of 406 mA h g<sup>-1</sup> has been achieved after 50 cycles at a current density of 0.2 C. Even at a larger current density of 0.5 C, our 1T-MoS<sub>2</sub> electrode achieved a capacity of 250.2 mA h g<sup>-1</sup>, exhibiting superior performance.

## 2. Experimental Section

### 2.1. Synthesis of MoS<sub>2</sub> Hollow Spheres

As with typical synthesis, 0.2 g of molybdenyl acetylacetonate was added into 30 mL of deionized water, stirring for about 30 min. Then, 0.4 g of thiourea was dissolved in the above solution. This reaction takes place at 200 °C for 12 h and is subsequently allowed to cool down naturally. After that, a black product was centrifuged and repeatedly rinsed with ethanol. Finally, the sample was dried at 70 °C under a vacuum overnight (1T-MoS<sub>2</sub>-200 at this stage). Following the above procedure, the samples were then heated at 600 °C for 2 h in an argon atmosphere resulting in 1T-MoS<sub>2</sub>-600.

### 2.2. Electrochemical Measurements

The working electrode was prepared by mixing the MoS<sub>2</sub>, acetylene black, and polyvinylidene fluoride (PVDF) (in a weight ratio of 7:2:1). Then, *N*-methylpyrrolidone (NMP) was used to dilute mixture to obtain a homogenous mud. 'The mud' was evenly spread on copper foil. Overnight, the foil was vacuum-dried at 110 °C. The sulfide-based solid electrolytes system was prepared by ball-milling 75% Li<sub>2</sub>S and 25% P<sub>2</sub>S<sub>5</sub> (molar percent) in inert Argon gas for about 24 h. At the same time, the counter electrode and reference electrode were composed of LiIn. A typical cell device was prepared using a cylinder, and the cell was pressed at 35 tons/cm<sup>2</sup> for 5 min after the enclosure was assembled in the glovebox. CV curves were captured in the working voltage range of 0.2–3 V at a scan rate of 0.2 mV s<sup>-1</sup> (EC-lab, VMP-300), and charge–discharge profiles were collected on the electrochemical analyzer at 25 °C (Hokuto Denko, HJ-SM8, Tokyo, Japan).

### 2.3. Characterization of the Samples

X-ray diffraction (XRD) (Rigaku, RINT-2200, CuKα, Tokyo, Japan) data was collected in 5–80° to characterize the crystallinity of the samples. An HR Evolution Raman system was employed to obtain Raman spectra (532 nm laser). The morphology of samples was observed by scanning electron microscope (SEM, Hitachi S4800). X-ray photoelectron spectroscopy (XPS) was performed in the range of 0–1200 eV to investigate the states of Mo and S.

### 3. Results and Discussion

Figure 1a shows the XRD patterns of 1T-MoS<sub>2</sub>-200 and 1T-MoS<sub>2</sub>-600. There are two peaks in the XRD pattern at 9.1° and 18.4° of 1T-MoS<sub>2</sub>-200, which could be assigned to the (002) and (004) planes, respectively. Approximately 0.95 nm was determined as the inter-layer spacing according to Bragg's Law equation. From Figure 1a, we can see 1T-MoS<sub>2</sub>-600 has shifted XRD peaks (at 13.8° and 26.5°). This is due to high-temperature annealing step which increased the crystallinity, resulting in reduced interplanar spacing [38]. However, the existence of (004) reflection for 1T-MoS<sub>2</sub>-600 at 26.5° indicates that the high temperature did not degrade the 1T-MoS<sub>2</sub> into its 2H-phase. To further support this claim, the Raman spectra of the two samples (Figure 1b) shows that the two samples share similar profiles. Specifically, a small peak at 375 cm<sup>-1</sup> is observed for a mode of 2H-MoS<sub>2</sub> in 1T-MoS<sub>2</sub>-600. A series of characteristic peaks at 110, 120, 144, 187, 207, 281, and 333 cm<sup>-1</sup> can be assigned to 1T-MoS<sub>2</sub> [39]. These results reveal that 1T phase 1T-MoS<sub>2</sub>-200 has not transitioned from to the 2H phase after annealing at 600 °C [40].

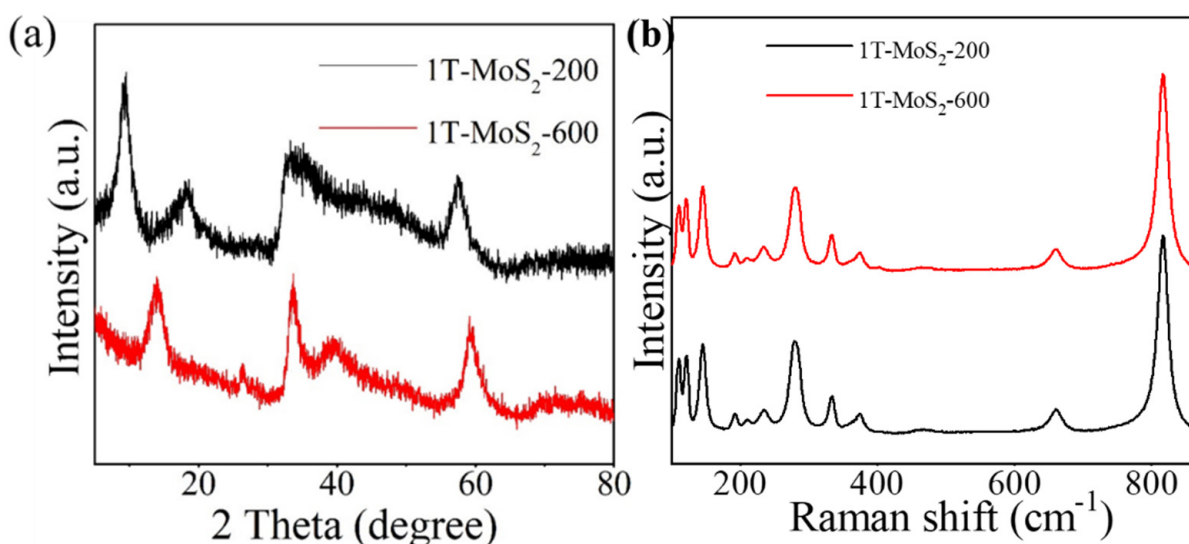


**Figure 1.** (a) XRD patterns, and (b) Raman spectra of 1T-MoS<sub>2</sub>-200 and 1T-MoS<sub>2</sub>-600, respectively.

In order to compare the carbon content of 1T-MoS<sub>2</sub>-600 with 1T-MoS<sub>2</sub>-200, the thermogravimetric (TG) information of the composite material 1T-MoS<sub>2</sub>-600 and 1T-MoS<sub>2</sub>-200 are presented in Figure S1. From the TG curves, the drop in weight before 200 °C is attributed to the evaporation of residues of organic matter and moisture in material. In the range of 200 to 350 °C [41], oxidation of both 1T-MoS<sub>2</sub>-600 and 1T-MoS<sub>2</sub>-200 contributed to the continued decrease in weight. Additionally, from the TG curves, the peak at 350–420 °C is a result of the combustion of carbon. The carbon amount in final composites doubtless were around 2.68% (1T-MoS<sub>2</sub>-600) and 10.5% (1T-MoS<sub>2</sub>-200). (The final product is MoO<sub>3</sub>).

XPS spectra was also employed to confirm the 1T-MoS<sub>2</sub> phase (Figure 2). The characteristic peaks of Mo and S was detected in the survey spectrum of 1T-MoS<sub>2</sub>-600 (Figure 2a). Figure 2b shows the distinct peaks of 1T-MoS<sub>2</sub> at 232.21 eV and 228.21 eV, which could be attributed to Mo 3d<sub>3/2</sub> and Mo 3d<sub>5/2</sub>, respectively. The binding energies at 233.01 and 229.33 eV result from the trace existence of 2H-MoS<sub>2</sub>. The binding energy at 226.42 eV is assigned to the feature peak of S 2p [42]. In comparison with the XPS spectra of 1T-MoS<sub>2</sub>-200 in Figure 2c, the results revealed that the transformation of the 1T phase is not significantly impacted by the high temperature, which is conform to the outcomes from Raman spectra and XRD.

SEM images were collected to penetrate the morphologies of MoS<sub>2</sub> samples, as shown in Figure 3. From Figure 3a, we can clearly see the spherical morphology of 1T-MoS<sub>2</sub>-200. The enlarged SEM image in Figure 3b reveals that the microspheres are composed of nanosheets with porous structures, which could suppress the volume change problem

in the lithiation/de-lithiation process [43]. Figure 3c,d show 1T-MoS<sub>2</sub>-600 after annealing. We can see that the 1T-MoS<sub>2</sub> still maintains its spherical morphology even after annealing, showing that 1T-MoS<sub>2</sub> can be stabilized at 600 °C.

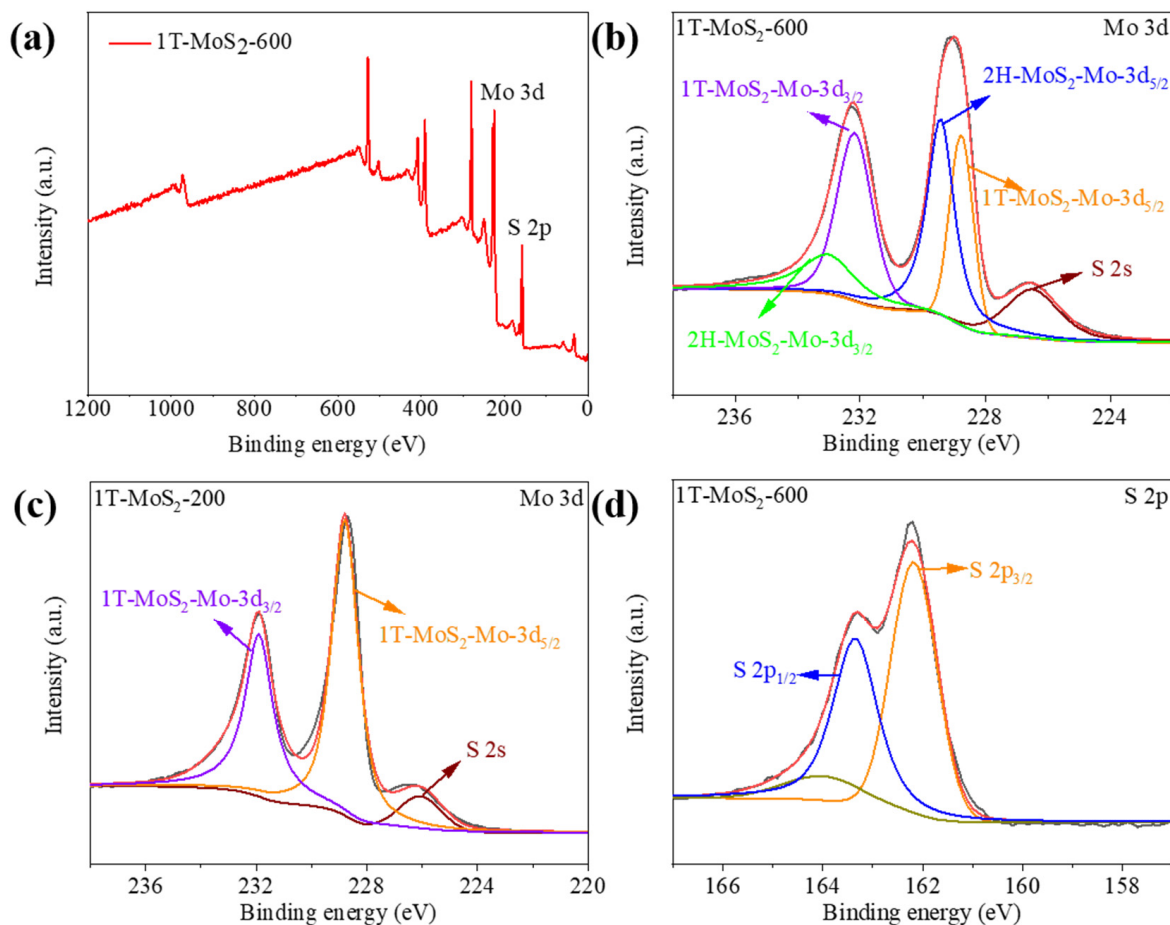


**Figure 2.** (a) XPS survey spectrum of 1T-MoS<sub>2</sub>-600, (b) Mo 3d spectrum of 1T-MoS<sub>2</sub>-600, (c) Mo 3d of 1T-MoS<sub>2</sub>-200, and (d) S 2p spectrum of 1T-MoS<sub>2</sub>-600.

Figure 4 displays TEM images of the 1T-MoS<sub>2</sub>-600. We can see that the 1T-MoS<sub>2</sub>-600 exhibits a micro-spherical morphology, composed of nanosheets. The presence of nanosheets is favorable for reducing the diffusion pathway of Li<sup>+</sup> and can improve the electrochemical performance. In Figure 4b, 1T-MoS<sub>2</sub>-600 has a lattice fringe of 0.95 nm (according to XRD data), which should be assigned to the (002) plane. In the magnified TEM image, the thin 1T-MoS<sub>2</sub>-600 can be seen and it benefits the diffusion of Li<sup>+</sup>. Expanded interlayer spacing of 1T-MoS<sub>2</sub>-600 and the layered structure promotes the diffusion of lithium ion [44]. Our TEM EDX images (Figure 4c–f) also shows a homogeneous Mo, S, and C element distribution in 1T MoS<sub>2</sub>-600. Then, we tested 1T-MoS<sub>2</sub>-600 and 1T-MoS<sub>2</sub>-200 electrochemical performances. As shown in Figure 5a, a stable capacity of 406 mA h g<sup>-1</sup> was obtained after 50 cycles for 1T-MoS<sub>2</sub>-600, while the capacity decayed quickly to 212.2 mA h g<sup>-1</sup> after few cycles for 1T-MoS<sub>2</sub>-200 (Figure S2). Even at 0.1 C, the capacity of 1T-MoS<sub>2</sub>-200 quickly degraded to 190 mA h g<sup>-1</sup> over a few cycles (Figure S3). These results imply that the increased crystallinity for 1T-MoS<sub>2</sub>-600 is leads to interfacial stability of ASSLIBs. The corresponding charge–discharge profiles of 1T-MoS<sub>2</sub>-600 at 0.2 C share a similar result, indicating a stable and reversible electrochemical process (Figure 5b). The rate performance of 1T-MoS<sub>2</sub>-600 has been checked at increasing current densities as shown in Figure 5c. At 0.1, 0.2, 0.5, and 1 C specific capacities of 538, 460, 376 and 296 mA h g<sup>-1</sup> were retained, respectively. A capacity of 424 mA h g<sup>-1</sup> is maintained as the

current density was returned to 0.2 C, exhibiting a superior rate performance. Figure 5d is charge–discharge profiles at varied current densities. There are prominent plateaus at varied charge–discharge curves, indicating that 1T-MoS<sub>2</sub>-600 has a better compatibility with the SEs, owing to its stable electrochemical kinetics.

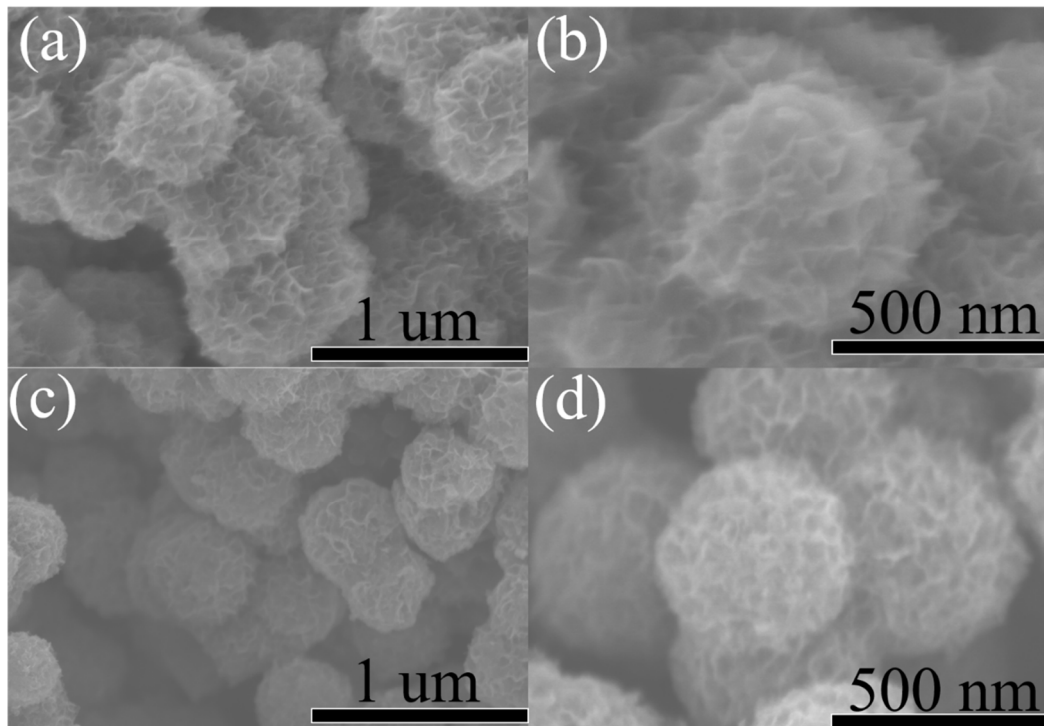


Figure 3. SEM images of (a,b)1T-MoS<sub>2</sub>-200 and (c,d) 1T-MoS<sub>2</sub>-600.

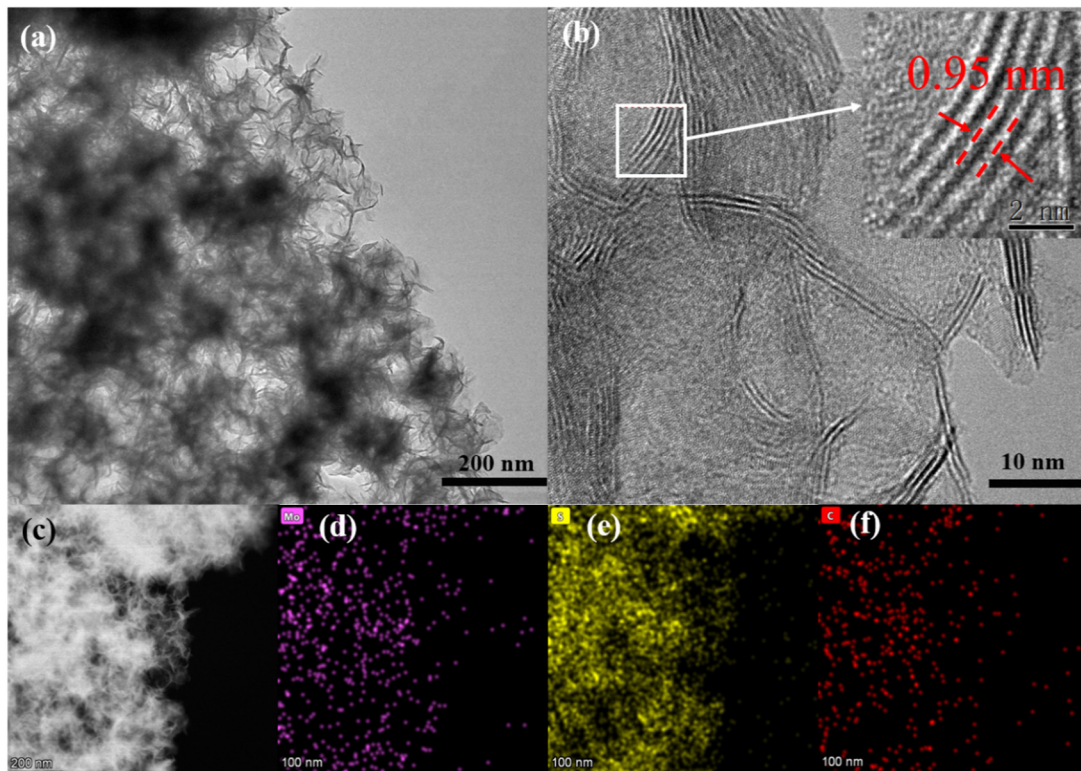
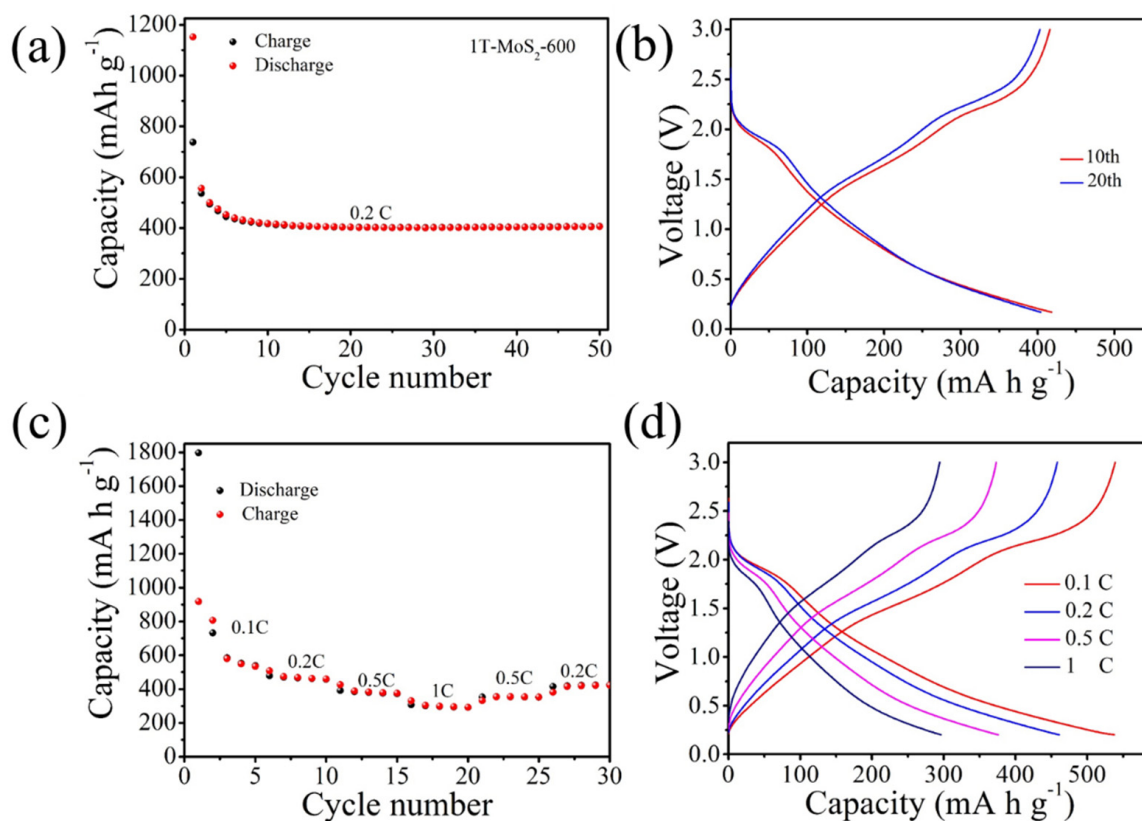


Figure 4. (a,b) TEM images and (c–f) STEM image and elemental mapping images of 1T-MoS<sub>2</sub>-600.



**Figure 5.** (a) Cycling performance of 1T–MoS<sub>2</sub>–600 at 0.2 C, (b) the corresponding charge–discharge profiles at 0.2 C, (c) rate performance of 1T–MoS<sub>2</sub>–600, and (d) the related charge–discharge profiles at varied current densities from 0.1 to 1 C.

To have an insight into the electrochemical kinetics, at the sweep rate of 0.2 mV s<sup>−1</sup>, the curves were performed. As demonstrated in Figure 6a, a broad peak appeared at 0.9 V in the first cathodic process, this might be demonstrated by the development of a solid electrolyte interlayer (SEI) and the insertion of Li<sup>+</sup> [45]. The cathodic peak at 0.2 V could be ascribed to the Li<sub>x</sub>MoS<sub>2</sub> being converted to Li<sub>2</sub>S and Mo [25]. The corresponding anodic peaks at 1.91 and 2.20 V are linked to the extraction of Li<sup>+</sup> and manufacture of MoS<sub>2</sub> [46]. In the subsequent cycles, the profiles are almost overlapping, signifying stable electrochemical kinetics. To investigate the capacitive contribution from the diffusion-controlled process and capacitance effect, CV curves at 0.2 to 1 mV s<sup>−1</sup> of stepwise-increasing sweep rate for 1T–MoS<sub>2</sub>–600 is plotted (Figure 6b). The dominant effect can be illustrated based on the following expression (1):

$$i = av^b \quad (1)$$

in which  $i$  and  $v$  represented the peak current and sweep rates, respectively.  $a$  and  $b$  are constants. When the value of  $b$  approached 0.5, the diffusion-controlled mechanism mostly affected the electrochemical process. By contrast, it was controlled by a capacitance effect when  $b$  was close to 1. The computed  $b$  values for the reduction and oxidation peaks were 0.73 and 0.78, respectively, as shown in Figure 6c. These values indicate that the cathodic and anodic processes are separately dominated by the diffusion process and capacitance effect. The specific ratio from the capacitance and diffusion-controlled process was estimated according to the subsequent expression (2):

$$i = k_1v + k_2v^{1/2} \quad (2)$$

where  $k_1$  and  $k_2$  represent the constant values, and  $i$  and  $v$  are the corresponding sweep rate and current. The capacitive contribution increased as the scan rates rose, as illustrated

in Figure 6d. More specifically, the contribution percentage from capacitance effect reached 70% at  $1 \text{ mV s}^{-1}$ . These findings demonstrate that, in comparison to a diffusion-controlled process, the pseudocapacitive effect has a greater impact on the electrochemical process.

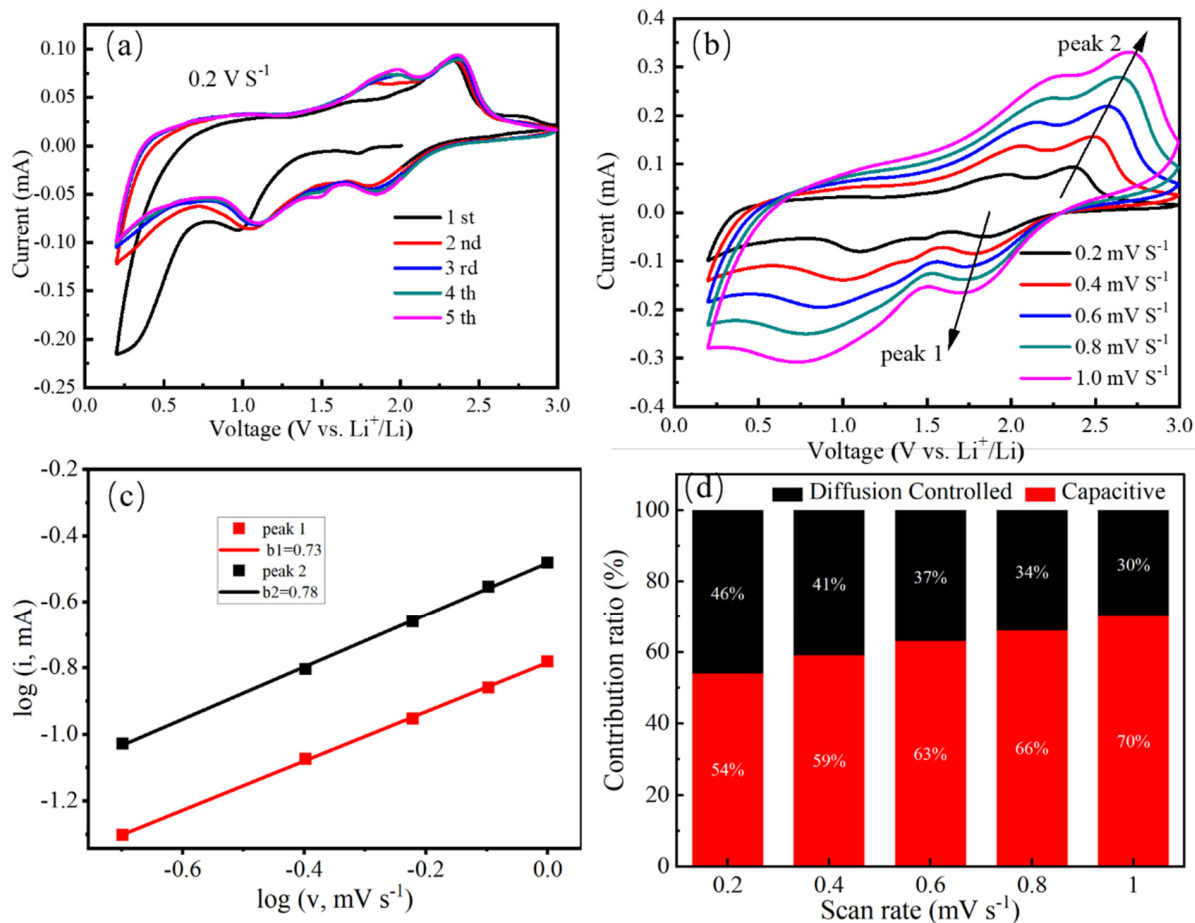


**Figure 6.** (a) CV curves of 1T-MoS<sub>2</sub>-600 at a sweep rate of  $0.5 \text{ mV s}^{-1}$ , (b) CV curves of 1T-MoS<sub>2</sub>-600 at different sweep rates, (c) b values from the oxidation and reduction peaks, and (d) the pseudocapacitive contribution of 1T-MoS<sub>2</sub>-600.

Ex situ XRD was used to monitor the reaction procedure of 1T-MoS<sub>2</sub>-600 during the lithiation/de-lithiation process. Figure 7 illustrates the initial state of 1T-MoS<sub>2</sub>-600 with two typical peaks at  $13.8^\circ$  (002) and  $32.6^\circ$  (100). As the discharging process takes place, the (002) plane signal becomes weaker and disappears completely at  $0.2 \text{ V}$  [47]. The weakening of the (002) signal peak is the result of intercalation of Li<sup>+</sup> and the conversion reaction of the 1T-MoS<sub>2</sub>-600. The peak did not appear in the succeeding charge process, suggesting that the 1T-MoS<sub>2</sub>-600 was already partially converted to the amorphous phase [48]. On the other hand, the peak of the (100) plane was recovered to a higher degree, corresponding to the de-lithiation and the reformation of MoS<sub>2</sub> process. However, we can see from Figure 7 that the peak of (100) plane did not recover back to its initial position before discharge. This might be due to the fact that some lithium was left in the crystal structure of 1T-MoS<sub>2</sub>-600. The following equations serve as a summary of the reaction mechanism (3–4):



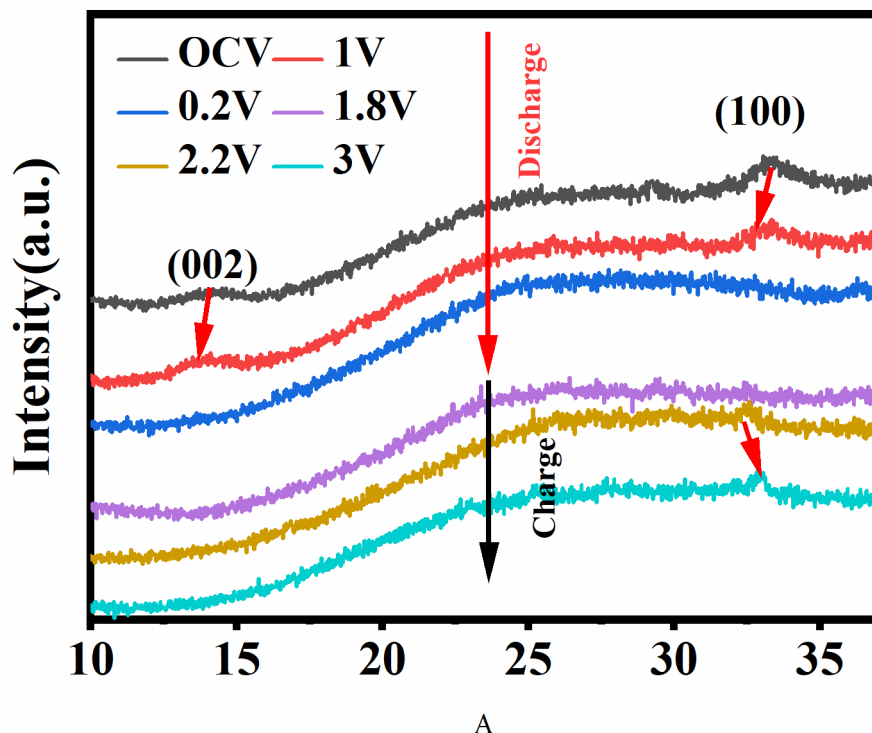


Figure 7. Ex situ XRD patterns of 1T-MoS<sub>2</sub>-600.

To further understand the electrochemical process, the electrochemical impedance spectra of 1T-MoS<sub>2</sub>-600 were tested at various temperatures (313, 323, 333, and 343 K), as illustrated in Figure 8. Based on the Arrhenius equation:

$$k = Ae^{-E_a/RT} \tag{5}$$

where  $k$  is the rate constant,  $R$  is the molar gas constant,  $T$  is the thermodynamic temperature,  $E_a$  is the apparent activation energy, and  $A$  is the pre-exponential factor.

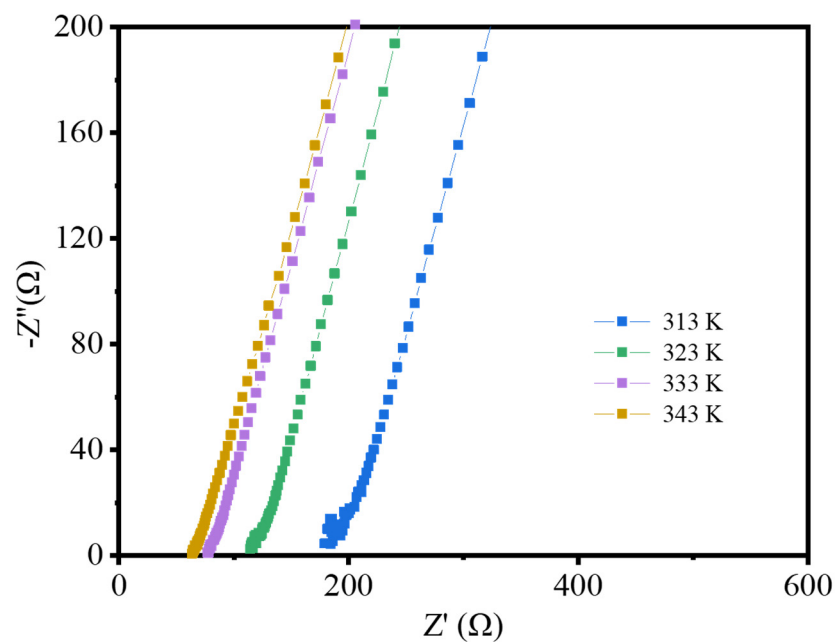


Figure 8. Electrochemical impedance spectra of 1T-MoS<sub>2</sub>-600 at an increasing temperature of 313, 323, 333, and 343 K, respectively.



We can linearize the equation to obtain the following expression:

$$\ln \frac{1}{R_{ct}} = \ln A_1 - \frac{E_a}{RT} \quad (6)$$

where  $R_{ct}$  is the charge transfer resistance,  $A_1$  is a constant,  $R$  is the molar gas constant,  $T$  is the temperature, and  $E_a$  is the activation energy. We obtained values for  $R_{ct}$  at different temperatures, and the  $E_a$  of 1T-MoS<sub>2</sub>-600 was determined to be 24.28 kJ mol<sup>-1</sup>, showing that the high crystalline 1T-phase of MoS<sub>2</sub> favors the electrochemical kinetics in ASSLIBs [49,50], so this material can demonstrate an outstanding cycling stability.

We also used galvanostatic intermittent titration technique (GITT) to analyze the diffusion efficiency of lithium-ion during the electrochemical process. Figure 9 shows the outcomes of the GITT curves for the 1T-MoS<sub>2</sub>-600 and 1T-MoS<sub>2</sub>-200 at 0.1 C. The calculation of diffusion coefficient was based on the following formula (7):

$$D_s = \frac{4}{\pi\tau} \left( \frac{n_m V_m}{S} \right)^2 \left( \frac{\Delta E_s}{\Delta E_t} \right)^2 \quad (7)$$

where  $\tau$  is the relaxation time,  $\Delta E_s$  and  $\Delta E_t$  come from steady voltage change and transient voltage variation in the discharge/charge process. We can see that 1T-MoS<sub>2</sub>-600 has a higher Li<sup>+</sup> diffusion than 1T-MoS<sub>2</sub>-200, indicating that the high crystallinity and the expanded (002) planes availed the compatibility between the electrode and SEs and the diffusion of Li<sup>+</sup> [51–53], so this material can demonstrate an outstanding cycling stability.

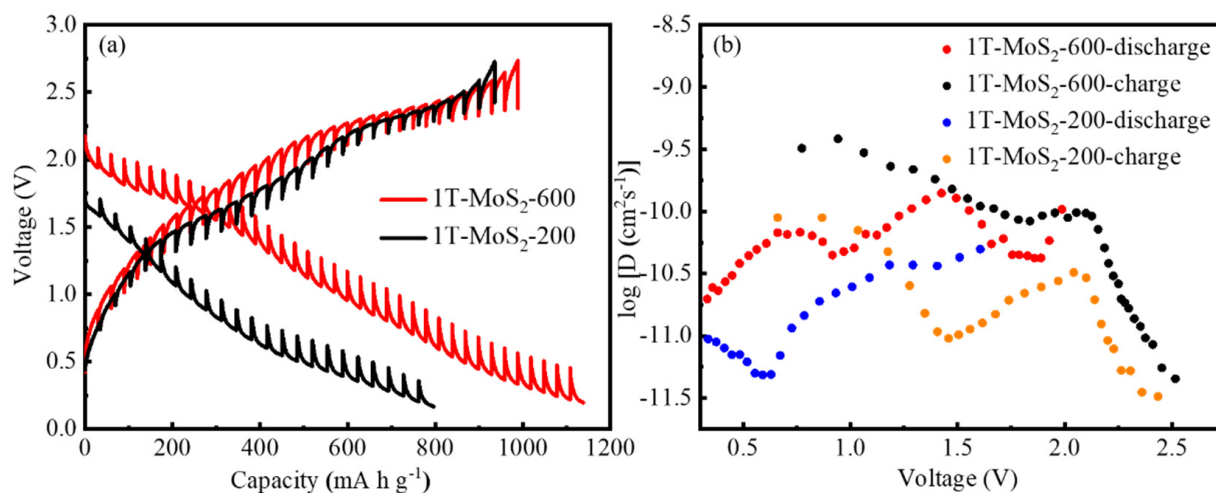


**Figure 9.** (a) The discharge–charge GITT plots at 0.1 C, and (b) lithium–ion diffusion coefficient of 1T–MoS<sub>2</sub>–600 and 1T–MoS<sub>2</sub>–200 at the discharge and charge processes, respectively.

Figure 10, which displays the performance of a few sulfide-based electrodes, further demonstrates the advantages of 1T-MoS<sub>2</sub>-600 in the matter of capacity and cycling stability. An outstanding performance of 1T-MoS<sub>2</sub>-600 compared to similar electrode materials demonstrates its immense potential for SSBs applications [34,54,55].

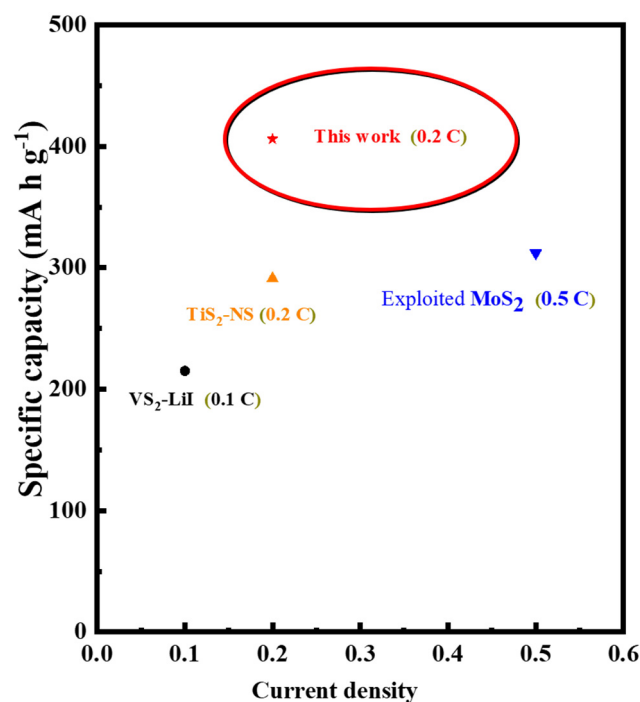


Figure 10. The cycling performance comparison of some sulfide-based electrode in ALLIBs.

#### 4. Conclusions

The incompatibility between electrodes and SEs is still an ongoing challenge that leads to poor electrochemical performance. In this work, 1T-MoS<sub>2</sub>-600 with high crystallinity was employed as an electrode in ASSLIBs and increased interfacial stability with SEs in ASSLIBs. Additionally, we overcame the bottleneck of 1T-MoS<sub>2</sub> degrading into its 2H phase at high temperatures by using a facile solvothermal synthesis method. We discovered and showed that this material demonstrated an outstanding cycling stability with a capacity of 406 mA h g<sup>-1</sup> after 50 cycles at a current density of 0.2 C. Even at a larger current density of 0.5 C, our 1T-MoS<sub>2</sub> electrode achieved a capacity of 250.2 mA h g<sup>-1</sup>, exhibiting superior performance. This work is also applicable to explore other electrode materials to solve interface issues in ASSLIBs.

**Supplementary Materials:** The following supporting information can be downloaded at: <https://www.mdpi.com/article/10.3390/batteries9010026/s1>, Figure S1: TG curves of 1T-MoS<sub>2</sub>-600 and 1T-MoS<sub>2</sub>-200; Figure S2: Cycling performance of 1T-MoS<sub>2</sub>-200 at 0.2C.; Figure S3: Cycling performance of 1T-MoS<sub>2</sub>-200 at 0.1 C.

**Author Contributions:** Conceptualization, Y.L., J.W. and M.W.; methodology, P.C.; software, J.W.; validation, Y.L., J.W. and M.W.; formal analysis, J.W.; Investigation, Z.Z. and K.W.; resources, J.W. and M.W.; data curation, P.C.; writing—original draft preparation, P.C.; writing—review and editing, W.Z., J.W. and M.W.; visualization, Y.L.; supervision, M.W.; project administration, J.W. and M.W.; funding acquisition, J.W. and M.W. All authors have read and agreed to the published version of the manuscript.

**Funding:** This research was supported by the Project of Science and Technology of Fuzhou City (Grant No. 2021-Y-080). J.W. acknowledges the Agency for Science, Technology and Research (Central Research Fund Award).

**Institutional Review Board Statement:** Not applicable.

**Informed Consent Statement:** Not applicable.

**Data Availability Statement:** Not applicable.

**Acknowledgments:** The authors thanks for the financial support from the Project of Science and Technology of Fuzhou City (Grant No. 2021-Y-080). J.W. acknowledges the Agency for Science, Technology and Research (Central Research Fund Award).

**Conflicts of Interest:** The authors declare no conflict of interest.

## References

1. Weiling, M.; Pfeiffer, F.; Baghernejad, M. Vibrational Spectroscopy Insight into the Electrode | electrolyte Interface/Interphase in Lithium Batteries. *Adv. Energy Mater.* **2022**, *12*, 2202504. [[CrossRef](#)]
2. Xu, J.; Cai, X.; Cai, S.; Shao, Y.; Hu, C.; Lu, S.; Ding, S. High-Energy Lithium Ion Batteries: Recent Progress and A Promising Future in Applications. *Energy Environ. Mater.* **2022**, 1–60. [[CrossRef](#)]
3. Oh, H.J.; Kang, H.K.; Ahn, H.; Park, J.; Choi, J.; Kim, H.Y.; Lee, E.; Yeo, S.Y.; Choi, Y.O.; Yeang, B.J.; et al. Layered oxide cathode-inspired secondary hard carbon microsphere anode material for high-power and long-life rechargeable batteries. *Chem. Eng. J.* **2023**, *454*, 140252. [[CrossRef](#)]
4. Wu, F.; Maier, J.; Yu, Y. Guidelines and trends for next-generation rechargeable lithium and lithium-ion batteries. *Chem. Soc. Rev.* **2020**, *49*, 1569–1614. [[CrossRef](#)]
5. Min, X.; Xu, G.; Xie, B.; Guan, P.; Sun, M.; Cui, G. Challenges of prelithiation strategies for next generation high energy lithium-ion batteries. *Energy Stor. Mater.* **2022**, *47*, 297–318. [[CrossRef](#)]
6. Gao, H.; Neale, A.R.; Zhu, Q.; Bahri, M.; Wang, X.; Yang, H.; Xu, Y.; Clowes, R.; Browning, N.D.; Little, M.A.; et al. A Pyrene-4,5,9,10-Tetraone-Based Covalent Organic Framework Delivers High Specific Capacity as a Li-Ion Positive Electrode. *J. Am. Chem. Soc.* **2022**, *144*, 9434–9442. [[CrossRef](#)]
7. Gao, H.; Tian, B.; Yang, H.; Neale, A.R.; Little, M.A.; Sprick, R.S.; Hardwick, L.J.; Cooper, A.I. Crosslinked Polyimide and Reduced Graphene Oxide Composites as Long Cycle Life Positive Electrode for Lithium-Ion Cells. *ChemSusChem* **2020**, *13*, 5571–5579. [[CrossRef](#)]
8. Lewis, J.A.; Cavallaro, K.A.; Liu, Y.; McDowell, M.T. The promise of alloy anodes for solid-state batteries. *Joule* **2022**, *6*, 1418–1430. [[CrossRef](#)]
9. Wang, L.; Sun, X.; Ma, J.; Chen, B.; Li, C.; Li, J.; Chang, L.; Yu, X.; Chan, T.-S.; Hu, Z.; et al. Bidirectionally Compatible Buffering Layer Enables Highly Stable and Conductive Interface for 4.5 V Sulfide-Based All-Solid-State Lithium Batteries. *Adv. Energy Mater.* **2021**, *11*, 2100881. [[CrossRef](#)]
10. Cao, D.; Zhao, Y.; Sun, X.; Natan, A.; Wang, Y.; Xiang, P.; Wang, W.; Zhu, H. Processing Strategies to Improve Cell-Level Energy Density of Metal Sulfide Electrolyte-Based All-Solid-State Li Metal Batteries and Beyond. *ACS Energy Lett.* **2020**, *5*, 3468–3489. [[CrossRef](#)]
11. Wang, J.; Okabe, J.; Urita, K.; Moriguchi, I.; Wei, M. Cu<sub>2</sub>S hollow spheres as an anode for high-rate sodium storage performance. *J. Electroanal. Chem.* **2020**, *874*, 114523. [[CrossRef](#)]
12. Oh, P.; Yun, J.; Choi, J.H.; Saqib, K.S.; Embleton, T.J.; Park, S.; Lee, C.; Ali, J.; Ko, K.; Cho, J. Development of High-Energy Anodes for All-Solid-State Lithium Batteries Based on Sulfide Electrolytes. *Angew. Chem. Int. Ed.* **2022**, *61*, e202201249. [[CrossRef](#)] [[PubMed](#)]
13. Wang, L.; Xie, R.; Chen, B.; Yu, X.; Ma, J.; Li, C.; Hu, Z.; Sun, X.; Xu, C.; Dong, S.; et al. In-situ visualization of the space-charge-layer effect on interfacial lithium-ion transport in all-solid-state batteries. *Nat. Commun.* **2020**, *11*, 5889. [[CrossRef](#)] [[PubMed](#)]
14. Wu, Y.; Zhou, K.; Ren, F.; Ha, Y.; Liang, Z.; Zheng, X.; Wang, Z.; Yang, W.; Zhang, M.; Luo, M.; et al. Highly reversible Li<sub>2</sub>RuO<sub>3</sub> cathodes in sulfide-based all solid-state lithium batteries. *Energy Environ. Sci.* **2022**, *15*, 3470–3482. [[CrossRef](#)]
15. Fan, Z.; Xiang, J.; Yu, Q.; Wu, X.; Li, M.; Wang, X.; Xia, X.; Tu, J. High Performance Single-Crystal Ni-Rich Cathode Modification via Crystalline LLTO Nanocoating for All-Solid-State Lithium Batteries. *ACS Appl. Mater. Interfaces* **2022**, *14*, 726–735. [[CrossRef](#)] [[PubMed](#)]
16. Yang, S.; Yamamoto, K.; Mei, X.; Sakuda, A.; Uchiyama, T.; Watanabe, T.; Takami, T.; Hayashi, A.; Tatsumisago, M.; Uchimoto, Y. High Rate Capability from a Graphite Anode through Surface Modification with Lithium Iodide for All-Solid-State Batteries. *ACS Appl. Energy Mater.* **2022**, *5*, 667–673. [[CrossRef](#)]
17. Tan, D.H.S.; Meng, Y.S.; Jang, J. Scaling up high-energy-density sulfidic solid-state batteries: A lab-to-pilot perspective. *Joule* **2022**, *6*, 1755–1769. [[CrossRef](#)]
18. Ohashi, A.; Kodama, M.; Xueying, S.; Hori, S.; Suzuki, K.; Kanno, R.; Hirai, S. Stress distribution in the composite electrodes of sulfide all-solid-state lithium-ion batteries. *J. Power Sources* **2020**, *470*, 228437. [[CrossRef](#)]
19. Gregory, G.L.; Gao, H.; Liu, B.; Gao, X.; Rees, G.J.; Pasta, M.; Bruce, P.G.; Williams, C.K. Buffering Volume Change in Solid-State Battery Composite Cathodes with CO<sub>2</sub>-Derived Block Polycarbonate Ethers. *J. Am. Chem. Soc.* **2022**, *144*, 17477–17486. [[CrossRef](#)] [[PubMed](#)]
20. Li, L.; Duan, H.; Zhang, L.; Deng, Y.; Chen, G. Optimized functional additive enabled stable cathode and anode interfaces for high-voltage all-solid-state lithium batteries with significantly improved cycling performance. *J. Mater. Chem. A* **2022**, *10*, 20331–20342. [[CrossRef](#)]
21. Ye, L.; Li, X. A dynamic stability design strategy for lithium metal solid state batteries. *Nature* **2021**, *593*, 218–222. [[CrossRef](#)] [[PubMed](#)]

22. Sun, Z.; Lai, Y.; Lv, N.; Hu, Y.; Li, B.; Jing, S.; Jiang, L.; Jia, M.; Li, J.; Chen, S.; et al. Boosting the Electrochemical Performance of All-Solid-State Batteries with Sulfide  $\text{Li}_6\text{PS}_5\text{Cl}$  Solid Electrolyte Using  $\text{Li}_2\text{WO}_4$ -Coated  $\text{LiCoO}_2$  Cathode. *Adv. Mater. Interfaces* **2021**, *8*, 2100624. [[CrossRef](#)]
23. Wan, H.; Zhang, J.; Xia, J.; Ji, X.; He, X.; Liu, S.; Wang, C. F and N Rich Solid Electrolyte for Stable All-Solid-State Battery. *Adv. Funct. Mater.* **2022**, *32*, 2110876. [[CrossRef](#)]
24. Li, Q.; Cao, Y.; Yin, G.; Gao, Y. The stable cycling of a high-capacity Bi anode enabled by an in situ-generated  $\text{Li}_3\text{PO}_4$  transition layer in a sulfide-based all-solid-state battery. *ChemComm* **2020**, *56*, 15458–15461. [[CrossRef](#)] [[PubMed](#)]
25. Priyadharsini, N.; Rupa Kasturi, P.; Shanmugavani, A.; Surendran, S.; Shanmugapriya, S.; Kalai Selvan, R. Effect of chelating agent on the sol-gel thermolysis synthesis of  $\text{LiNiPO}_4$  and its electrochemical properties for hybrid capacitors. *J. Phys. Chem. Solids* **2018**, *119*, 183–192. [[CrossRef](#)]
26. Priyadharsini, N.; Shanmugapriya, S.; Kasturi, P.R.; Surendran, S.; Selvan, R.K. Morphology-dependent electrochemical properties of sol-gel synthesized  $\text{LiCoPO}_4$  for aqueous hybrid capacitors. *Electrochim. Acta* **2018**, *289*, 516–526. [[CrossRef](#)]
27. Gao, Y.; Hai, P.; Liu, L.; Yin, J.; Gan, Z.; Ai, W.; Wu, C.; Cheng, Y.; Xu, X. Balanced Crystallinity and Nanostructure for  $\text{SnS}_2$  Nanosheets through Optimized Calcination Temperature toward Enhanced Pseudocapacitive  $\text{Na}^+$  Storage. *ACS Nano* **2022**, *16*, 14745–14753. [[CrossRef](#)]
28. Geng, P.; Zheng, S.; Tang, H.; Zhu, R.; Zhang, L.; Cao, S.; Xue, H.; Pang, H. Transition Metal Sulfides Based on Graphene for Electrochemical Energy Storage. *Adv. Energy Mater.* **2018**, *8*, 1703259. [[CrossRef](#)]
29. Priyadharsini, N.; Shanmugavani, A.; Surendran, S.; Senthilkumar, B.; Vasylechko, L.; Kalai Selvan, R. Improved electrochemical performances of  $\text{LiMnPO}_4$  synthesized by a hydrothermal method for Li-ion supercapacitors. *J. Mater. Sci. Mater. Electron.* **2018**, *29*, 18553–18565. [[CrossRef](#)]
30. Zhang, Y.; Zhang, L.; Lv, T.A.; Chu, P.K.; Huo, K. Two-Dimensional Transition Metal Chalcogenides for Alkali Metal Ions Storage. *ChemSusChem* **2020**, *13*, 1114–1154. [[CrossRef](#)]
31. Yin, X.; Tang, C.S.; Zheng, Y.; Gao, J.; Wu, J.; Zhang, H.; Chhowalla, M.; Chen, W.; Wee, A.T.S. Recent developments in 2D transition metal dichalcogenides: Phase transition and applications of the (quasi-)metallic phases. *Chem. Soc. Rev.* **2021**, *50*, 10087–10115. [[CrossRef](#)] [[PubMed](#)]
32. Sun, Q.; Li, D.; Dai, L.; Liang, Z.; Ci, L. Structural Engineering of  $\text{SnS}_2$  Encapsulated in Carbon Nanoboxes for High-Performance Sodium/Potassium-Ion Batteries Anodes. *Small* **2020**, *16*, 2005023. [[CrossRef](#)] [[PubMed](#)]
33. Wang, H.; Yuan, Q.; Wang, D.; Chen, G.; Cheng, X.; Kups, T.; Schaaf, P. Disordered surface formation of  $\text{WS}_2$  via hydrogen plasma with enhanced anode performances for lithium and sodium ion batteries. *Sustain. Energy Fuels* **2019**, *3*, 865–874. [[CrossRef](#)]
34. Santhosha, A.L.; Nayak, P.K.; Pollok, K.; Langenhorst, F.; Adelhelm, P. Exfoliated  $\text{MoS}_2$  as Electrode for All-Solid-State Rechargeable Lithium-Ion Batteries. *J. Phys. Chem. C* **2019**, *123*, 12126–12134. [[CrossRef](#)]
35. Li, S.; Liu, Y.; Zhao, X.; Cui, K.; Shen, Q.; Li, P.; Qu, X.; Jiao, L. Molecular Engineering on  $\text{MoS}_2$  Enables Large Interlayers and Unlocked Basal Planes for High-Performance Aqueous Zn-Ion Storage. *Angew. Chem. Int. Ed.* **2021**, *60*, 20286–20293. [[CrossRef](#)]
36. Mirabal, N.; Aguirre, P.; Santa Ana, M.A.; Benavente, E.; González, G. Thermal stability and electrical conductivity in polyethers-molybdenum disulfide nanocomposites. *Electrochim. Acta* **2003**, *48*, 2123–2127. [[CrossRef](#)]
37. Wang, Y.; Yang, Y.; Zhang, D.; Wang, Y.; Luo, X.; Liu, X.; Kim, J.-K.; Luo, Y. Inter-overlapped  $\text{MoS}_2/\text{C}$  composites with large-interlayer-spacing for high-performance sodium-ion batteries. *Nanoscale Horiz.* **2020**, *5*, 1127–1135. [[CrossRef](#)]
38. Bai, J.; Zhao, B.; Zhou, J.; Si, J.; Fang, Z.; Li, K.; Ma, H.; Dai, J.; Zhu, X.; Sun, Y. Glucose-Induced Synthesis of 1T- $\text{MoS}_2/\text{C}$  Hybrid for High-Rate Lithium-Ion Batteries. *Small* **2019**, *15*, 1805420. [[CrossRef](#)]
39. Zhuo, Y.; Prestat, E.; Kinloch, I.A.; Bissett, M.A. Self-Assembled 1T- $\text{MoS}_2$ /Functionalized Graphene Composite Electrodes for Supercapacitor Devices. *ACS Appl. Energy Mater* **2022**, *5*, 61–70. [[CrossRef](#)]
40. Jiang, Y.; Li, S.; Zhang, F.; Zheng, W.; Zhao, L.; Feng, Q. Metal-semiconductor 1T/2H- $\text{MoS}_2$  by a heteroatom-doping strategy for enhanced electrocatalytic hydrogen evolution. *Catal. Commun.* **2021**, *156*, 106325. [[CrossRef](#)]
41. Fayed, M.G.; Attia, S.Y.; Barakat, Y.F.; El-Shereafy, E.E.; Rashad, M.M.; Mohamed, S.G. Carbon and nitrogen co-doped  $\text{MoS}_2$  nanoflakes as an electrode material for lithium-ion batteries and supercapacitors. *SM&T* **2021**, *29*, e00306.
42. Acerce, M.; Vohry, D.; Chhowalla, M. Metallic 1T phase  $\text{MoS}_2$  nanosheets as supercapacitor electrode materials. *Nat. Nanotechnol.* **2015**, *10*, 313–318. [[CrossRef](#)] [[PubMed](#)]
43. Liu, B.; Wang, L.; Zhu, Y.; Peng, H.; Du, C.; Yang, X.; Zhao, Q.; Hou, J.; Cao, C. Ammonium-Modified Synthesis of Vanadium Sulfide Nanosheet Assemblies toward High Sodium Storage. *ACS Nano* **2022**, *16*, 12900–12909. [[CrossRef](#)] [[PubMed](#)]
44. Zhang, X.; Weng, W.; Gu, H.; Hong, Z.; Xiao, W.; Wang, F.; Li, W.; Gu, D. Versatile Preparation of Mesoporous Single-Layered Transition-Metal Sulfide/Carbon Composites for Enhanced Sodium Storage. *Adv. Mater.* **2022**, *34*, 2104427. [[CrossRef](#)] [[PubMed](#)]
45. Yu, X.; Zhao, G.; Huang, H.; Liu, C.; Lyu, P.; Zhang, N. Interlayer-expanded  $\text{MoS}_2$  nanoflowers anchored on the graphene: A high-performance  $\text{Li}^+/\text{Mg}^{2+}$  co-intercalation cathode material. *Chem. Eng. J.* **2022**, *428*, 131214. [[CrossRef](#)]
46. Lu, H.; Tian, K.; Bu, L.; Huang, X.; Li, X.; Zhao, Y.; Wang, F.; Bai, J.; Gao, L.; Zhao, J. Synergistic effect from coaxially integrated  $\text{CNTs}@\text{MoS}_2/\text{MoO}_2$  composite enables fast and stable lithium storage. *J. Energy Chem.* **2021**, *55*, 449–458. [[CrossRef](#)]
47. Li, S.; Liu, Y.; Zhao, X.; Shen, Q.; Zhao, W.; Tan, Q.; Zhang, N.; Li, P.; Jiao, L.; Qu, X. Sandwich-Like Heterostructures of  $\text{MoS}_2/\text{Graphene}$  with Enlarged Interlayer Spacing and Enhanced Hydrophilicity as High-Performance Cathodes for Aqueous Zinc-Ion Batteries. *Adv. Mater.* **2021**, *33*, 2007480. [[CrossRef](#)]

48. Gong, F.; Ye, S.; Liu, M.; Zhang, J.; Gong, L.; Zeng, G.; Meng, E.; Su, P.; Xie, K.; Zhang, Y.; et al. Boosting electrochemical oxygen evolution over yolk-shell structured O-MoS<sub>2</sub> nanoreactors with sulfur vacancy and decorated Pt nanoparticles. *Nano Energy* **2020**, *78*, 105284. [[CrossRef](#)]
49. Zhou, L.-F.; Gao, X.-W.; Du, T.; Gong, H.; Liu, L.-Y.; Luo, W.-B. New Phosphate Zn<sub>2</sub>Fe(PO<sub>4</sub>)<sub>2</sub> Cathode Material for Nonaqueous Zinc Ion Batteries with Long Life Span. *ACS Appl. Mater. Interfaces* **2022**, *14*, 8888–8895. [[CrossRef](#)] [[PubMed](#)]
50. Wang, J.; Huang, J.; Huang, S.; Komine, Y.; Notohara, H.; Urita, K.; Moriguchi, I.; Wei, M. Regulating the effects of SnS shrinkage in all-solid-state lithium-ion batteries with excellent electrochemical performance. *Chem. Eng. J.* **2022**, *429*, 132424. [[CrossRef](#)]
51. Wu, D.; Sun, F.; Qu, Z.; Wang, H.; Lou, Z.; Wu, B.; Zhao, G. Multi-scale structure optimization of boron-doped hard carbon nanospheres boosting the plateau capacity for high performance sodium ion batteries. *J. Mater. Chem. A* **2022**, *10*, 17225–17236. [[CrossRef](#)]
52. Zhang, W.; Li, H.; Zhang, Z.; Xu, M.; Lai, Y.; Chou, S.-L. Full Activation of Mn<sup>4+</sup>/Mn<sup>3+</sup> Redox in Na<sub>4</sub>MnCr(PO<sub>4</sub>)<sub>3</sub> as a High-Voltage and High-Rate Cathode Material for Sodium-Ion Batteries. *Small* **2020**, *16*, 2001524. [[CrossRef](#)] [[PubMed](#)]
53. Tao, L.; Yang, Y.; Wang, H.; Zheng, Y.; Hao, H.; Song, W.; Shi, J.; Huang, M.; Mitlin, D. Sulfur-nitrogen rich carbon as stable high capacity potassium ion battery anode: Performance and storage mechanisms. *Energy Stor. Mater.* **2020**, *27*, 212–225. [[CrossRef](#)]
54. Oh, D.Y.; Choi, Y.E.; Kim, D.H.; Lee, Y.-G.; Kim, B.-S.; Park, J.; Sohn, H.; Jung, Y.S. All-solid-state lithium-ion batteries with TiS<sub>2</sub> nanosheets and sulphide solid electrolytes. *J. Mater. Chem. A* **2016**, *4*, 10329–10335. [[CrossRef](#)]
55. Wang, J.; Okabe, J.; Komine, Y.; Notohara, H.; Urita, K.; Moriguchi, I.; Wei, M. The optimized interface engineering of VS<sub>2</sub> as cathodes for high performance all-solid-state lithium-ion battery. *Sci. China Technol. Sci.* **2022**, *65*, 1859–1866. [[CrossRef](#)]

**Disclaimer/Publisher's Note:** The statements, opinions and data contained in all publications are solely those of the individual author(s) and contributor(s) and not of MDPI and/or the editor(s). MDPI and/or the editor(s) disclaim responsibility for any injury to people or property resulting from any ideas, methods, instructions or products referred to in the content.